FULL PAPER

Stress change generated by the 2019 İstanbul–Silivri earthquakes along the complex structure of the North Anatolian Fault in the Marmara Sea

Murat Şahin[1*] , Cenk Yaltırak[1], Fatih Bulut[2] and Aslı Garagon[2]

Abstract

The North Anatolian Fault Zone is a dextral system operating between the Eurasian and Anatolian plates in northern Turkey. Across the Marmara Sea south of İstanbul, it deforms at ~18 mm/year slip rate, where the statistics of historical earthquakes suggest that a few M7+ earthquakes are generated every ~250 years. Currently, M7+ earthquakes are overdue as this section of the fault has not been reactivated since the 1766 and 1754 earthquakes. In this frame, identifying the stress change by the 2019 M5.8 İstanbul–Silivri earthquake is essential to characterize its influence on the critically stressed Marmara Sea segments of the North Anatolian Fault Zone. To do this, we mapped not only the main segments but also the secondary faults in the vicinity of the 2019 M5.8 İstanbul–Silivri earthquake to locate the fault patch it reactivated, as well as to accurately model the fault segments, where it significantly changed the stress. The joint analysis of relocated hypocenters and the Coulomb stress modeling shows that the mainshock failed a SW–NE striking splay fault, generating a stress increase of up to three bars on the fault that has the potential to generate M7+ earthquake.

Keywords: The Marmara Sea, 2019 İstanbul–Silivri earthquakes, North Anatolian Fault Zone, Coulomb Stress Change

Graphical Abstract

---

*Correspondence: sahinmurat2@itu.edu.tr

[1] Department of Geological Engineering, Faculty of Mines, Istanbul Technical University, Istanbul, Turkey
Full list of author information is available at the end of the article

Şahin *et al. Earth, Planets and Space* (2022) 74:167
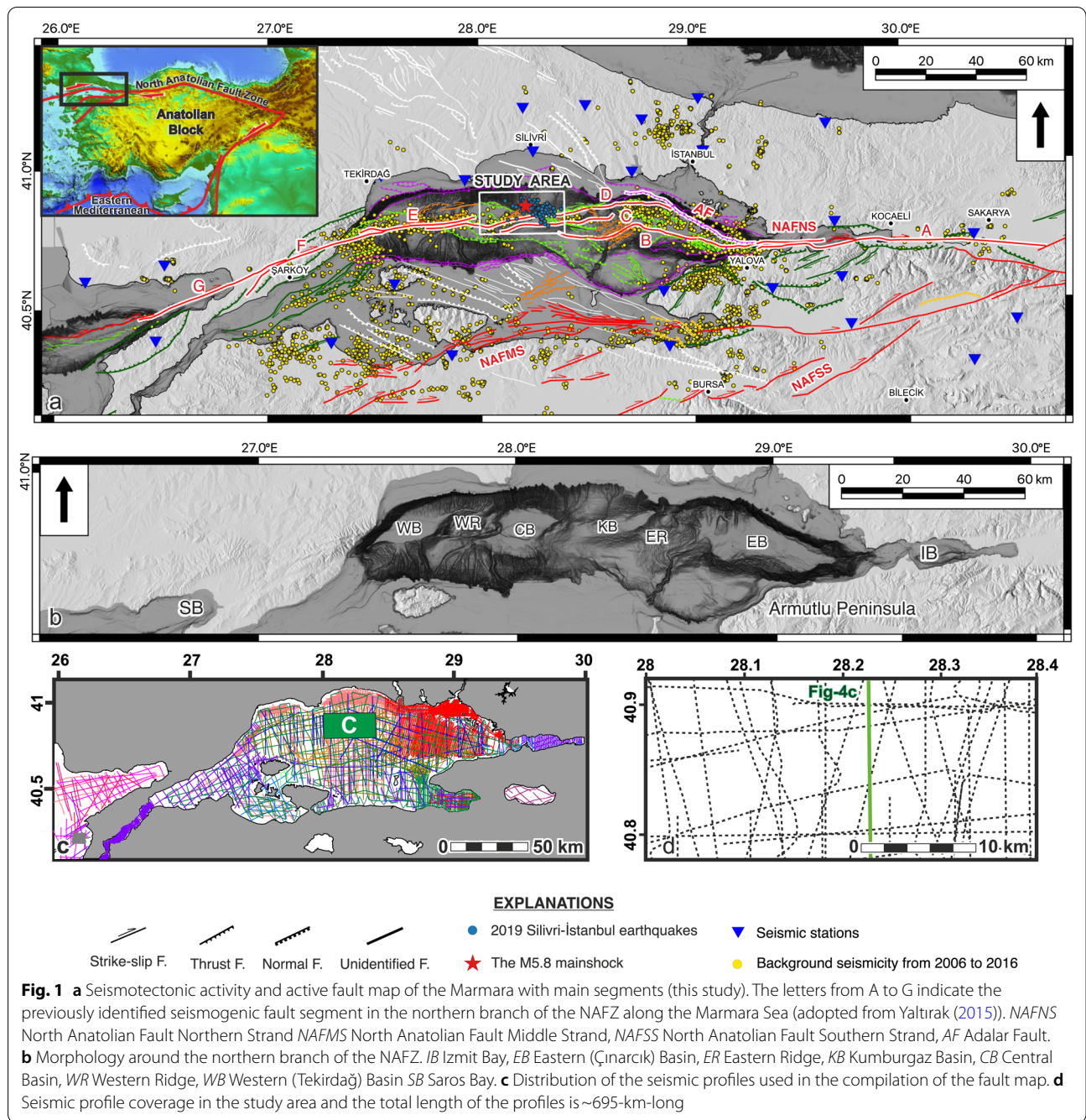
Page 2 of 16
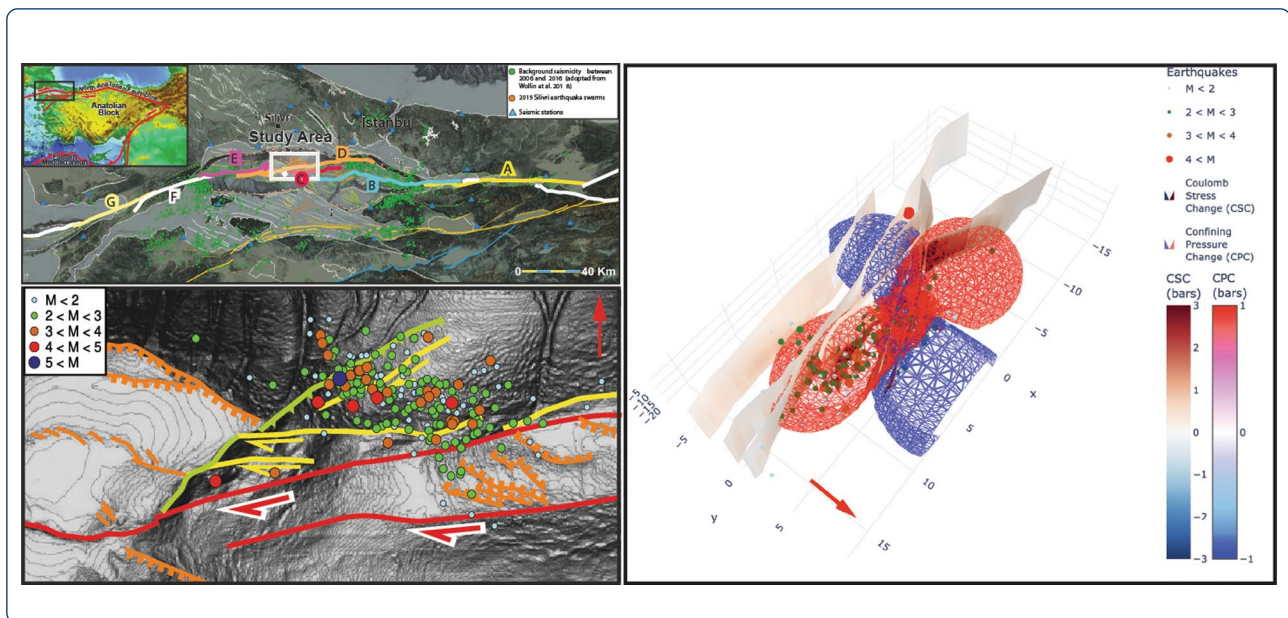
Introduction

The North Anatolian Fault Zone (NAFZ) is a dextral fault (Ketin 1948) acting as a plate boundary between the Eurasian and Anatolian plates (Şengör 1979). It extends for ~1500 km from the Karlıova triple junction in the east towards the northern Aegean Sea in the west, forming a remarkably narrow north-convex zone across Anatolia. Near the east of the Marmara Sea, the NAFZ splits into three main strands, namely, the northern, middle, and southern branches (Barka 1992; Yaltırak 2002). In this region, the NAFZ can be described to have formed a multi-segmented horsetail structure (Yaltırak 2002). Although all three branches have been active during the Plio-Quaternary, most of the historical and recent slip occurs along the northern branch (Le Pichon et al. 2001). The northern branch enters the Izmit Bay, extends across the entire Marmara Sea, and reaches the Aegean Sea through the Ganos Fault through the Gelibolu Peninsula (Fig. 1a, b).

The tens of km-long section of the northern branch of the NAFZ in the west has been silent for not a few decades (Egeran and Lahn 1944, 1948; Ketin 1948). In August 1912 and 1999, two M7+ earthquakes have reactivated the westernmost and easternmost sections of the Marmara Sea on the northern branch of the NAFZ (Barka et al. 2002; Altınok et al. 2003; Aksoy et al. 2010), and the remaining unruptured section of the northern branch in the Marmara Sea has been thoroughly investigated for the seismic hazard assessment (Hubert-Ferrari et al. 2000; Parsons et al. 2000; Parsons 2004; Armijo et al. 2005; Pondard et al. 2007; Bulut et al. 2019). Parsons (2004) conducted a study based on the attenuation laws

and historical intesity data to allocate the reported major historical earthquakes (Fig. 2a). Furthermore, several fault scarps (1.5–50-m-high) in the south of the Central and Tekirdağ basins and ~6-m-long dextral-slip in the Western High have been reported (Armijo et al. 2005). The authors reported that eastern tip of the 1912 rupture terminated in the south of the Central Basin based on these recent observations and the high sedimentation rate in the Marmara Sea (Figs. 1b and 2b). Yaltırak (2015) presented the distribution of major historical earthquakes based on the reported felt area, and Bulut et al. (2019) reported three segments that could generate M7+ earthquakes by relying on the slip-deficit and historical observations (Fig. 2c). The location of the historical earthquakes is still a matter of debate. Nevertheless, the majority of the researchers are in agreement with the location of the May 1766 earthquake (1766a in Fig. 2).
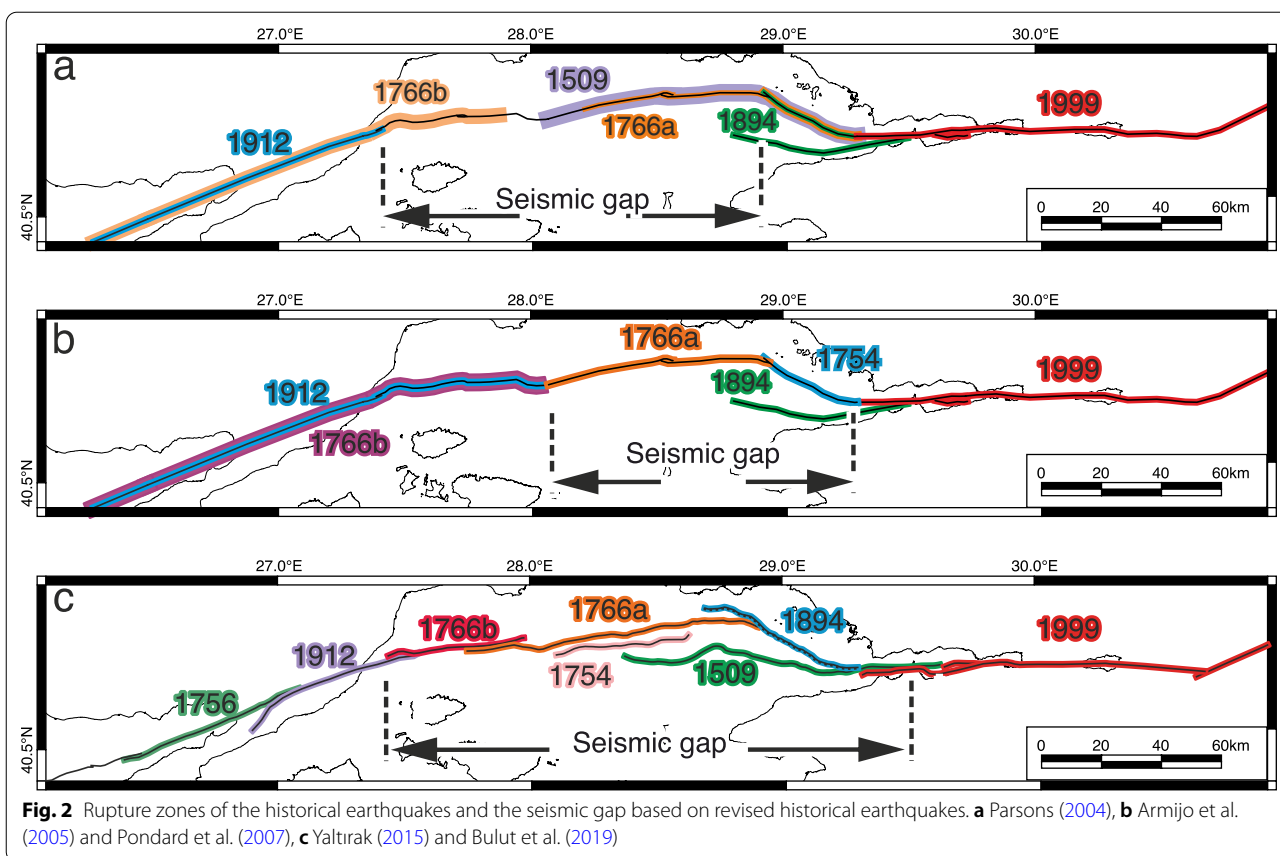
26 September 2019 M5.8 İstanbul–Silivri earthquake and its M4.7 foreshock on 24 September 2019 occurred in close proximity to the main fault, which previously failed in May 1766 and currently has the potential to generate M7+ earthquake within this highly inhabited region (Bulut et al. 2019). The M5.8 mainshock, which generated non-negligible structural damage in western İstanbul, preceded a precursory M4.7 earthquake and its aftershocks. In addition, two more earthquakes (M4.7 and M4.2) occurred in the same area in 2020.

We investigated a 32-km section of the Marmara seismic gap in the vicinity of these earthquakes (Figs. 1a and 2). As no faults had been yet identified in the hypocentral zone (e.g., Le Pichon et al. 2001; Armijo et al. 2002; Şengör et al. 2014) except for the study by Yaltırak (2002),

Şahin *et al. Earth, Planets and Space*   (2022) 74:167

Page 3 of 16

Fig. 1 a Seismotectonic activity and active fault map of the Marmara with main segments (this study). The letters from A to G indicate the previously identified seismogenic fault segment in the northern branch of the NAFZ along the Marmara Sea (adopted from Yaltırak (2015)). *NAFNS* North Anatolian Fault Northern Strand *NAFMS* North Anatolian Fault Middle Strand, *NAFSS* North Anatolian Fault Southern Strand, *AF* Adalar Fault. **b** Morphology around the northern branch of the NAFZ. *IB* Izmit Bay, *EB* Eastern (Çınarcık) Basin, *ER* Eastern Ridge, *KB* Kumburgaz Basin, *CB* Central Basin, *WR* Western Ridge, *WB* Western (Tekirdağ) Basin *SB* Saros Bay. **c** Distribution of the seismic profiles used in the compilation of the fault map. **d** Seismic profile coverage in the study area and the total length of the profiles is ~695-km-long

that mapped two internally parallel faults to the north of the main fault zone offshore Silivri (Additional file 1: Fig. S1), we investigated active faults in the vicinity of these earthquakes using seismic reflection profiles. Based on the previously published fault map of Le Pichon et al. (2001), Irmak et al. (2021), and Karabulut et al. (2021) analyzed and interpreted the Silivri earthquakes. Karabulut et al. (2021) suggested that a WNW–ESE striking 60°NE dipping causative fault is deeply buried below the

thick sedimentary cover in the Marmara Basin. Irmak et al. (2021) also noted that the Silivri earthquakes did not occur on the Main Marmara Fault and suggested that existing secondary structures were likely responsible for the mainshock. Finally, the authors concluded that the observed seismic activity could best be explained by the pre-existing N89°W oriented 33°NE dipping thrust fault within a sinistral stepover across a transpressional region on the NAFZ.

Şahin *et al. Earth, Planets and Space*   (2022) 74:167

Page 4 of 16

Fig. 2 Rupture zones of the historical earthquakes and the seismic gap based on revised historical earthquakes. **a** Parsons (2004), **b** Armijo et al. (2005) and Pondard et al. (2007), **c** Yaltırak (2015) and Bulut et al. (2019)

In this study, we provide a new perspective that first identifies the seismically active faults in the vicinity of the 2019 M5.8 event and its M4.7 foreshock, and in a second step, characterizes the stress change it generated on these newly identified faults and the faults that capable to generate M7+ earthquake. According to this study, the 2019 Silivri earthquakes took place on a secondary fault system located slightly off the main fault zone in the north. This secondary fault system was mapped for the first time in this study using the seismic reflection profiles. Stress interaction between the faults and their effects on each other, the distribution of the earthquakes around fault planes, and the relationship between the focal mechanism solutions and fault planes are provided in the interactive form as an additional file. This will allow the readers to visually distinguish the differences between earthquake occurrence mechanisms suggested in recent studies (Irmak et al. 2021; Karabulut et al. 2021) and the result of this study.

Materials and database

Our primary objective is to characterize the spatiotemporal behavior of the foreshock and aftershock activities of the M5.8 mainshock and understand the physical process behind these earthquake activities. This requires the identification of the geometries and kinematics of the seismically active faults and the accurate determination of the earthquake hypocenters. To identify the geometries of the seismically active faults, we combined seismic reflection profiles and multibeam seafloor bathymetry mosaics. To accurately locate earthquake hypocenters, we combined all available seismograph data in the region operated by Kandilli Observatory and Earthquake Research Institute and also Disaster and Emergency Management Presidency of Turkey (Fig. 1a).

The seismic reflection profiles were partially compiled from the previously published studies (Aksu et al. 2000; Siyako et al. 2000; Yaltırak and Alpar 2002; Ateş et al. 2003; Parke et al. 2003; Carton et al. 2007; Demirbağ et al. 2007; Kurt and Yücesoy 2009; Sorlien et al. 2012; Vardar et al. 2014; Okay and Aydemir 2016; Steckler et al. 2018), but also include unpublished data that reside in various government institutions (Fig. 1c). These seismic profiles consist of > 20,000 line-km of single- and multi-channel data, with penetration ranging between 0.25 and 10 s in

Şahin *et al. Earth, Planets and Space*   (2022) 74:167

Page 5 of 16

two-way travel time (TWT). The seafloor bathymetry was obtained from multibeam data collected by Ifremer (Rangin et al. 2001) and ONHO (Turkish Navy Office of Navigation, Hydrography, and Oceanography). These data were integrated with single-beam sonar data across the shallow water areas to create the best possible spatial coverage of the seafloor for delineating the surface traces of seismically active faults in the Marmara Sea. These seismic reflection profiles and bathymetric data were imported into Petrel™ software. The dense grid of seismic reflection profiles with ~2.5-km line spacing allowed the compilation of a very detailed fault map (Fig. 1a, c, and Additional file 1: Fig. S2).

We visually interpreted the seismic reflection profiles to identify the fault traces. We started the interpretation from the shallow reflection profiles (penetrates up to 0.25 s in TWT) to determine which fault traces delineate the seafloor. Then we mapped these fault traces by following the correspondent deformation structures on the seismic reflection profiles and bathymetric images (Fig. 3a). The bathymetric images were generated with various illumination source settings and colors to capture lineaments and deformation-related features. Finally, we extended the mapped fault traces in depth using the seismic profiles that reach up to 8–10 s (Additional file 1: Figs. S3 and S4) in TWT by considering the consistency of the fault structures on the seismic profiles. We also included fault traces that do not delineate the seafloor in our fault map by mapping the similar fault structures around the fault traces in reflection profiles. To obtain an average 1 km spatial resolution of the 3D fault map in the lateral direction, we generated 1 km equally spaced N–S trending 360+ traverse profiles containing the topographic information for the Marmara region (Fig. 3a). We digitized the fault surfaces on these profiles by considering the morphologic features and apparent dip angle of the fault trace that was interpreted from at least two seismic reflection profiles in the east and west of the traverse profile.

Since there is no open-source 3D velocity model published for the whole Marmara Sea, the depth migration of the mapped 3D fault surfaces was carried out using the crustal models across the Marmara Sea (Gürbüz et al. 2000; Karabulut et al. 2002; Bulut et al. 2009; Tary et al. 2011; Bayrakçı et al. 2013; Batsi et al. 2018) up to 20-km-depth which is in agreement with the depth of the background seismicity of the Marmara Sea (Wollin et al. 2018; Bulut et al. 2019). We derived the root-mean-square (rms) velocities from these crustal models and converted them into interval velocities using the Dix conversion (Dix 1955). After, we generated an interval velocity—TWT function using a second-order polynomial fit and used this function to calculate the depth of

each node on the fault surfaces (Fig. 3b). Here we present a section of this map and 3D fault model in the vicinity of the mainshock (40.775°–40.925° N and 28°–28.4° E), showing the detailed structural architecture of the Silivri earthquake area (Fig. 4). Using the slightly different crustal models did not significantly change the geometry or location of the faults in the seismic profiles. However, we used Bulut et al. (2009) crustal model for depth migration of the fault surfaces in this specified region as well as for hypocenter locations to make them comparable.

The seismological data set consists of hypocenters of 214 M1.3+ relocated earthquakes and fault plane solutions of 14 M3+ earthquakes (Additional file 1: Table S1). Fault plane solutions were obtained using P-wave first motion polarities based our hypocenter locations. Using FOCMEC algorithm developed by Snoke (2003), the first motion polarities were projected onto a focal sphere to discriminate between compressional and tensional quadrants. The boundaries between these quadrants verify the geometry of an activated fault and the direction of slip it accommodates. We used the double-difference method (Waldhauser and Ellsworth 2000) to relocate the earthquakes accurately, which uses relative arrival times to minimize unknown path effects on location accuracy. For travel time modeling, we used the 1D crustal velocity model by Bulut et al. (2009). Relative arrival times were determined using the waveform cross-correlation technique rather than to refine relative arrival times. We used only cross-correlation derived differential travel times, and the data is weighted using cross-correlation coefficients. We investigated relative locations of a total of 217 earthquakes forming 13,992 earthquake pairs and consequently analyzed 110,998 differential travel times, and the average link per earthquake pair is 15. Furthermore, we used both P- and S-waves to constrain hypocentral depths better. There are three seismic stations less than 25 km from the focal area (Fig. 1a). Under these monitoring conditions, we could accurately constrain the epicenters and the hypocentral depths. The sampling rate of forty seismic stations is 100 Hz. Excluding three of them, they are equipped with broadband seismographs. This setup allows recording the frequency contents up to 50 Hz. Under these circumstances, harmonics below 35 Hz are recorded sufficiently. According to the lambda-over-four rule (Geller and Mueller 1980), this allows hypocentral precision up to 43 m. Combining these improvements, we obtained 76 m average spatial accuracy for 214 relative hypocenter locations (Additional file 1: Fig. S5). The size of the earthquake cluster we analyzed is 15 by 8 km and the average error of our initial absolute hypocenters are 1.4 and 1.7 km in the horizontal and vertical axis, respectively. In addition, the double difference earthquake relocation algorithm has an
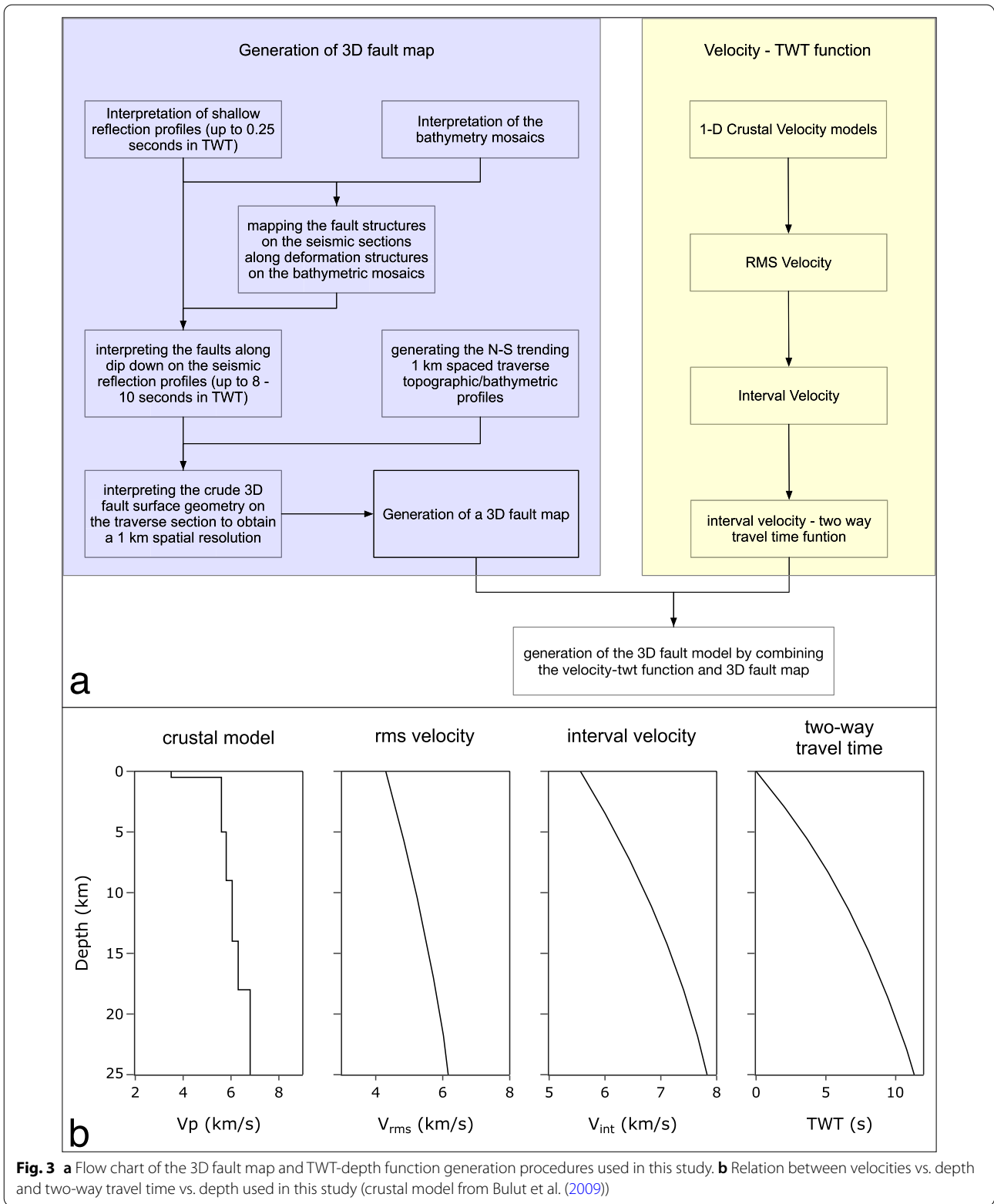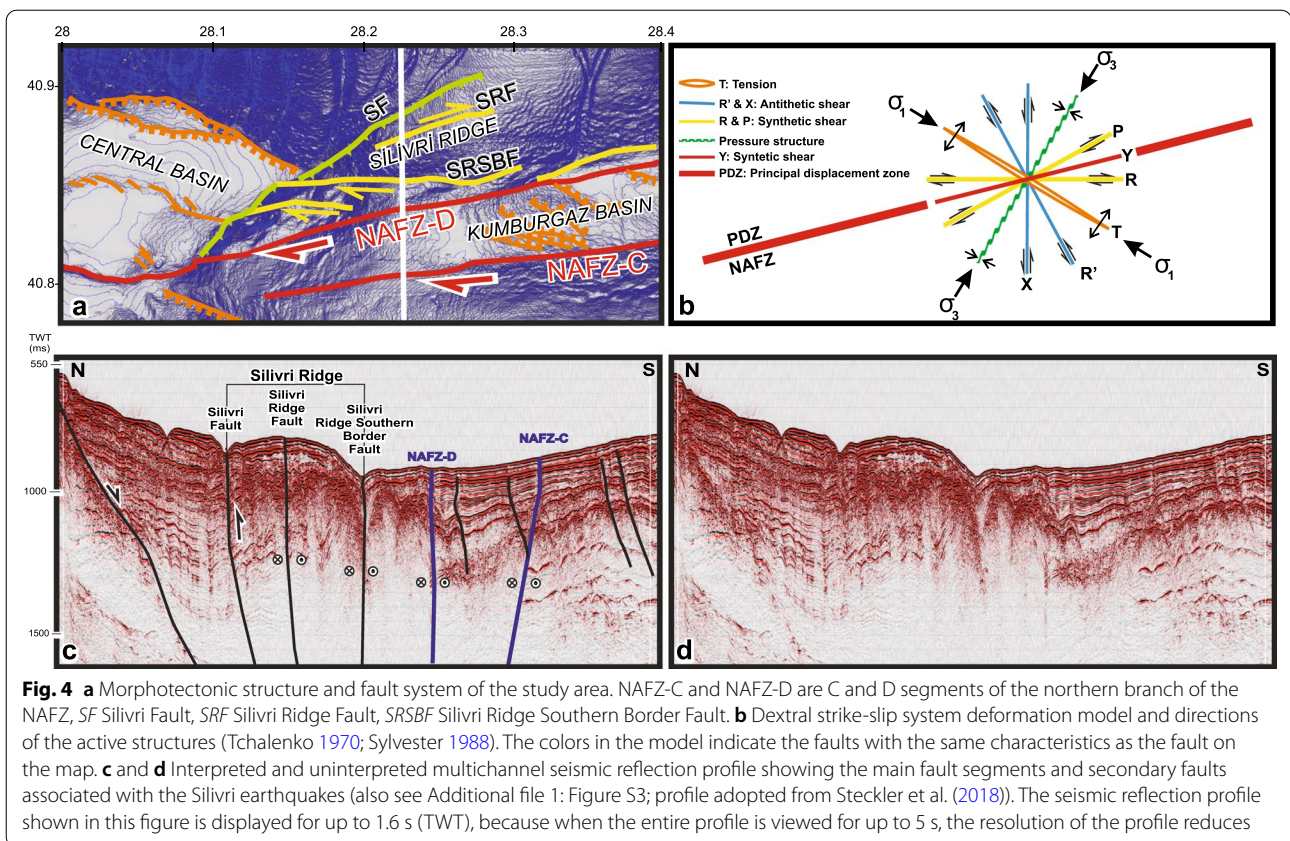
Fig. 3 **a** Flow chart of the 3D fault map and TWT-depth function generation procedures used in this study. **b** Relation between velocities vs. depth and two-way travel time vs. depth used in this study (crustal model from Bulut et al. (2009))

Fig. 4 **a** Morphotectonic structure and fault system of the study area. NAFZ-C and NAFZ-D are C and D segments of the northern branch of the NAFZ, *SF* Silivri Fault, *SRF* Silivri Ridge Fault, *SRSBF* Silivri Ridge Southern Border Fault. **b** Dextral strike-slip system deformation model and directions of the active structures (Tchalenko 1970; Sylvester 1988). The colors in the model indicate the faults with the same characteristics as the fault on the map. **c** and **d** Interpreted and uninterpreted multichannel seismic reflection profile showing the main fault segments and secondary faults associated with the Silivri earthquakes (also see Additional file 1: Figure S3; profile adopted from Steckler et al. (2018)). The seismic reflection profile shown in this figure is displayed for up to 1.6 s (TWT), because when the entire profile is viewed for up to 5 s, the resolution of the profile reduces

additional constraint to keep the centroid of the earthquake cluster, which substantially improves the accuracy of initial absolute locations, in addition to the accuracy of relative locations (Waldhauser and Ellsworth 2000). In this context, our double difference derived earthquake locations are capable of identifying structures on sub-kilometer scale, which is sufficient to confirm that the 2019 Silivri earthquakes mostly failed off-fault structures at a distance of 1–7 km from the main fault.

To investigate any possible interaction between the 2019 Silivri earthquakes and the northern branch of the NAFZ, the spatiotemporal behavior and focal mechanism solutions of the earthquakes are presented as interactive figures (Additional file 1: Figs. S6, S7, and S8). In these figures, we also present the fault plane solutions and earthquake hypocenter locations from two recent studies (Durand et al. 2020; Karabulut et al. 2021) generated using different crustal velocity models to display the coherence with our 3D fault model.

Structural setting

The study area is located on the WSW–ENE trending middle section of the dextral NAFZ in the Marmara Sea (Figs. 1d and 4a). According to Tchalenko (1970), this trend of dextral fault zone must be characterized by E–W

striking R shears, NE–SW striking P shears, NNE–SSW striking compressional, and NW–SE striking tensional structures (Fig. 4b). In the study area, based on our observations from seismic reflection sections and bathymetry mosaics, the northern branch of the NAFZ consists of two main faults that are subparallel to each other (NAFZ-D and NAFZ-C in Fig. 4a; segment C deviates ~4° in the clockwise direction from D), where several small fault segments developed with a strike deviated ~14° in the counterclockwise from the trend of the NAFZ-D. One of the two main faults is named Main Marmara Fault by Le Pichon et al. (2001) or the Kumburgaz segment (indicated as segment D in Fig. 1a, NAFZ-D; (Yaltırak 2015)). The second main fault (or NAFZ-C), located ~4 km to the south of the NAFZ-D, represents the southern border of the Kumburgaz Basin (Fig. 4b, red-colored lines). The ~80°N dipping Silivri Ridge Southern Border Fault represents R shear, while the 80°SE-dipping Silivri Ridge Fault represents P shear (Fig. 4a, b, yellow-colored lines). The NW–SE striking normal faults are well correlated with tensional structures (Fig. 4a, b, orange-colored lines). In addition, the NE–SW striking 75°SE dipping Silivri Fault is a dextral oblique thrust fault, and it is

Şahin *et al. Earth, Planets and Space*   (2022) 74:167

Page 8 of 16

well correlated with the expected compressional trend (Fig. 4a, b, green-colored lines). This fault network, which is well resolved by the seismic profiles, represents a typical kinematic architecture in strike-slip systems (Tchalenko 1970).

The intra-basinal and shallow normal faults have substantially deviated from the long axis of the Kumburgaz Basin (Fig. 4a), which clearly shows that the Kumburgaz Basin is bounded in the north and south by two dextral-lateral faults (Fig. 4a, c). This horsetail fault system, consisting of P and R shears and the associated compressional and tensional structures, can generate a diffused view of the seismicity rather than a narrow alignment on a single fault if they activate simultaneously or successively.

Seismic activity

The relocated Silivri earthquake distribution displays a diffuse view in the north of the NAFZ. This diffuse view in the seismicity is well correlated with the mapped faults, and the spatial allocation of the M4+ earthquakes coincides with the secondary fault surfaces in the north of NAFZ (Fig. 5 and Additional file 1: Fig. S6). Therefore, the spatiotemporal distribution of the relocated earthquake hypocenters indicates that three individual faults have been activated during the 2019 Silivri earthquakes. The M4.7 foreshock activated the dextral Silivri Ridge Fault on September 24, 2019, and was followed 51 h later by the M5.8 mainshock activating the Silivri Fault to the north (Fig. 5a, Additional file 1: Fig. S6; Table S1). On the same day, the Silivri Ridge Southern Border Fault in the south and the Silivri Fault in the north have been activated, generating two M4.1 earthquakes (Fig. 5a and Additional file 1: Fig. S6). After that, the seismicity progressively migrated towards the main fault segment beneath the Silivri Ridge. The aftershock activity decayed after an M4.7 earthquake developed in the west of Silivri Ridge Southern Border Fault on January 11, 2020, and the area became completely silent after the M4.2 and the M3.6 earthquakes on September 24, 2020 (Fig. 5a, Additional file 1: Fig. S6; Table S1). These two 2020 earthquakes, of which fault plane solutions are dominantly dextral strike-slip, have occurred between NAFZ-D and Silivri Ridge Southern Border Fault (Additional file 1: Fig. S6).

The planes on the source mechanism solutions around the Silivri Fault revolve in the same direction as the surface trace of the Silivri Fault (Fig. 5a). Since the faults are modeled as a non-planar surface in this study, a slight deviation (up to 15-degree) in the surface trace of the fault and focal mechanism solution is expected (Additional file 1: Fig. S6). The Silivri Ridge Fault (SRF) and Silivri Ridge Southern Border Fault (SRSBF) seems in

agreement with focal mechanism solutions in their vicinity as well (Fig. 5a and Additional file 1: Fig. S6). The kinematic analysis of the fault planes mapped from seismic reflection profiles and the kinematic analysis of the planes obtained from the source mechanism solutions of M4+ earthquakes are compatible with each other in the main stress direction, as shown in Fig. 5b.

In summary, the 2019 Silivri earthquakes appear to have been distributed along the Silivri Ridge Fault, Silivri Fault, and Silivri Ridge Southern Border Fault that we have identified to the north of the NAFZ-D (Fig. 5 and Additional file 1: Fig. S6). Based on our observations, they do not simply represent a WNW–ESE-striking single fault (Karabulut et al. 2021) or a sinistral stepover transpressional zone (Irmak et al. 2021). Instead, the 2019 Silivri earthquakes suggest physical interaction between these three faults (Additional file 1: Figs. S6, S7, and S8). We further investigated these interactions using the Coulomb stress modeling based on identified fault geometries and fault plane solutions.

Coulomb stress change

We simulated Coulomb stress change associated with the 2019 Silivri earthquakes to investigate the effect of the seismic activity on the main fault (NAFZ-C and NAFZ-D) as well as the interaction between the fault network and the regional seismic activity using Relax v1.0.7 (Barbot and Fialko 2010a, b). The stress modeling was performed in two steps. In the first step, we simulated Coulomb stress change within the fault network in response to M4+ earthquakes in 2019 (Additional file 1: Table S1). In the second step, we calculated the ratio between the stress change generated by M4+ earthquakes and the existing stress on the faults (Fig. 3).

For stress modeling, the fault planes were divided into 1×1 km patches. The rake of each patch on the source fault was calculated using the principal axes of local deformation (Örgülü 2011) by implementing the Slicken v1.0 algorithm (Xu et al. 2017) in Python programing language to perform Coulomb stress calculations. The mean slips of the earthquakes were calculated from the earthquakes' magnitudes and dimensions of the ruptured faults (Hanks and Kanamori 1979) by assuming that the entire fault surface was ruptured. The slip distribution of each earthquake was modeled by modifying the calculated mean slips using k-square (Gallovič and Brokešová 2004), bulls-eye (Mildon et al. 2016), and uniform distributions. Our calculations show that the difference between the Coulomb results obtained from the apparent friction coefficient range of 0.3–0.5 is negligible (up to 10% difference) (Beeler et al. 1996). Therefore, we provide the results for the friction coefficient of 0.4 in this paper;
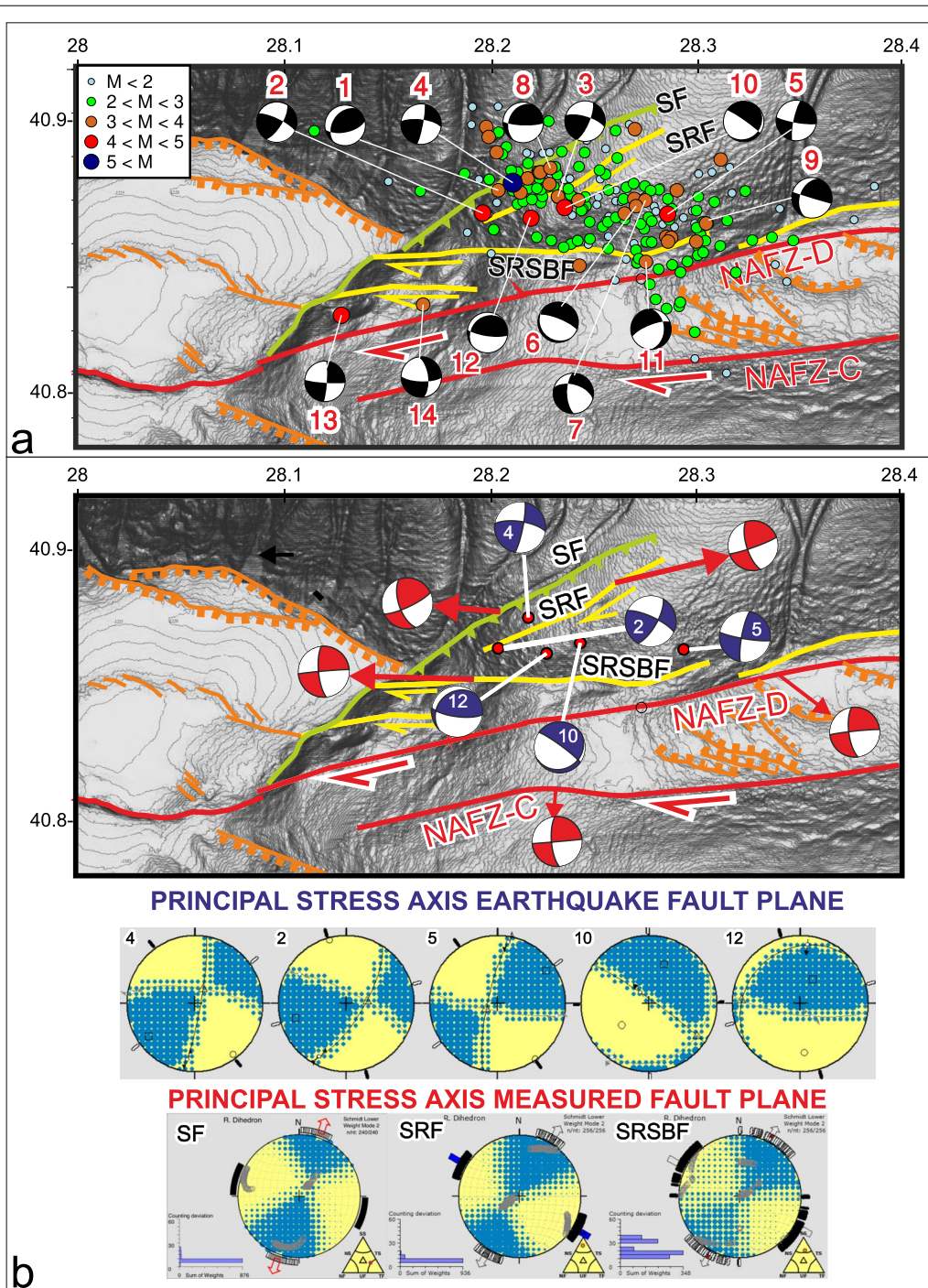
Şahin *et al. Earth, Planets and Space*   (2022) 74:167

Page 9 of 16

Fig. 5 **a** Distribution of the 2019 Silivri earthquakes. The numbers with source mechanism solutions are from Additional file 1: Table S1. Green-colored lines show dextral oblique thrust faults, yellow- and red-colored lines show dextral strike-slip, and orange-colored lines stand for normal faults. **b** Correlation of kinematic analysis of the source mechanism solution (in dark blue color) and fault planes (in red color)

the rest can be found in the additional file (Additional file 1: Figs. S9 and S10).

The existing stress on the faults before the 2019 Silivri earthquakes was estimated using the slip deficit (Bulut et al. 2019) on the NAFZ-C and NAFZ-D. Here, we further detail this slip deficit model taking into account the slip partitioning between sub-parallel fault segments. Bulut et al. (2019) previously assumed a single main fault in the vicinity of

Şahin *et al. Earth, Planets and Space*   (2022) 74:167

Page 10 of 16

the 2019 Silivri earthquakes, while we now spread this slip deficit to the NAFZ-C and NAFZ-D segments, which failed different times, in 1754 and 1766, respectively (Yaltırak 2015). The pre-Coulomb stress on the non-planar fault system in the vicinity of the 2019 Silivri earthquakes was calculated using the slip deficit-derived inter-seismic slip potential of the main fault segments (Mildon et al. 2019). The pre-Coulomb stress on the fault surface was modified using coseismic Coulomb stress change by the 2019 Silivri earthquakes.

The accuracy of pre-Coulomb stress rate distribution is dependent on the time span from the last earthquake up to today, the slip-deficit rate along the fault surfaces, and the geometry of the source and receiver fault surfaces. The accuracies of the historical seismicity and slip-deficit rate have been discussed (Yaltırak 2015; Bulut et al. 2019). The accuracy of the implementation of the introduced historical information and slip deficit on the modeled fault surfaces for the stress calculations is %10 as a response to 15° changes in the orientation of the fault patch.

The M4.7 foreshock and its aftershock activity associated with the Silivri Ridge Fault caused ~0.9 bars of stress increase in the region, where the M5.8 mainshock nucleated on the Silivri Fault 51 h later (Fig. 6b and Additional file 1: Fig. S9). The foreshock activity generated 1.5 bars of stress increase on the Silivri Ridge Southern Border Fault (Fig. 6b). It also generated ~0.1 bars stress increase on the NAFZ-D and below 0.1 bars stress increase on the NAFZ-C (Fig. 6b and Additional file 1: Fig. S9). The results suggest that the stress increase on the Silivri Fault triggered the M5.8 mainshock, and the mainshock generated 3+bars of stress increase on all of the secondary faults in the vicinity of the earthquake hypocenter (Fig. 6b, c). The M4+after-shocks generated minor stress perturbation on the receiver faults remaining below 0.1 bars (Fig. 6d, e, and Additional file 1: Fig. S9). The overall activity generated 3.4 bars of Coulomb stress increase on the NAFZ-D (Fig. 6, Additional file 1: Figs. S8, and S9). This corresponds to 10% of the pre-loaded stress increase on the NAFZ-D (Fig. 6f and Additional file 1: Fig. S10). The stress increase on Silivri Ridge Fault and Silivri Ridge Southern Border Fault is above 10% of the inter-seismic storage. This probably triggered the M4.7 earthquake on January 11, 2020 (Fig. 5, Additional file 1: Fig. S6; Table S1).

The pore pressure change is a function of the change in confining pressure (Barbot 2014). The change in the confining pressure in the area in response to the mainshock is given in Additional file 1: Fig. S11. There, the distribution of aftershock activity agrees with the increased confining pressure (1+bars), indicating that the mainshock has increased the pore pressure along, where the aftershocks occurred. This agreement between the spatial allocation of the aftershocks and increased confining pressure in the 3D medium provides evidence that the mainshock took place on the SE-dipping Silivri Fault.

Discussion

Le Pichon et al. (2001) suggested the presence of a single, thoroughgoing, active dextral strike-slip system occupying the central axis of the Marmara Sea extending from the Izmit Bay in the east and Ganos Fault in the west (Additional file 1: Fig. S1a). Armijo et al. (2002) suggested a multi-segmented pull-apart model (Additional file 1: Fig. S1b). Both of these studies were conducted on the same seismic reflection data (Le Pichon et al. 2001; Armijo et al. 2002). On the other hand, Yaltırak (2002) suggested a multi-segmented horsetail fault structure for the Marmara Sea using different seismic reflection data (Additional file 1: Fig. S1c). The single thoroughgoing fault has been thoroughly discussed (e.g., Yaltırak 2002; Armijo et al. 2005). Various recent studies used this single, thoroughgoing dextral strike-slip fault as the starting point of their investigation of the Silivri earthquakes (e.g., Irmak et al. 2021; Karabulut et al. 2021). Unfortunately, the previously published fault maps show no fault in where Silivri earthquakes occurred (Le Pichon et al. 2001; Armijo et al. 2002; Şengör et al. 2014), although several published seismic sections show a fault zone in the region of interest (Okay et al. 2000) a fault was proposed based on two different kinematic models by the recent studies (Irmak et al. 2021; Karabulut et al. 2021). Karabulut et al. (2021) interpreted the WNW–ESE trending alignment of the 2019 Silivri earthquakes to represent *"relatively-old-hidden structures which are not observed on the seismicity and seismic images"* (see their Fig. 6). In principle, W–E striking dextral system operates as a normal fault in case it deviates NW–SE orientation (Tchalenko 1970; Fig. 4b). However, Karabulut et al. (2021) observed instead predominantly reverse components. In this context, the 2019 Silivri earthquakes require a 3D investigation to understand the rupturing process they represent at depth. Irmak et al. (2021) argued that the 2019 Silivri

(See figure on next page.)

Fig. 6 Panel–I show the snapshots of the seismic activity up to the given date-time stamp on the individual map. **a** Seismic activity up to M4.7 foreshock, **b** M5.8 mainshock **c**, and **d** M4.1 aftershocks. Panel–II shows the current stress and stress change on the fault surfaces in response to M4+ earthquakes given in Panel–I. **a** Pre-Coulomb stress, **b** M4.7 foreshock on September 24, **c** the M5.8 mainshock on September 26, **d** and **e** M4.1 aftershocks on September 26, 2019, f) the ratio between the total stress change in response to M4+ earthquakes and pre-Coulomb stress. The slip distribution of the source faults was selected k-square for this figure. *SF* Silivri Fault, *SRF* Silivri Ridge Fault, *SRSBF* Silivri Ridge Southern Border Fault, *NAFZ-C* and *NAFZ-D* the segments of the northern branch of NAFZ
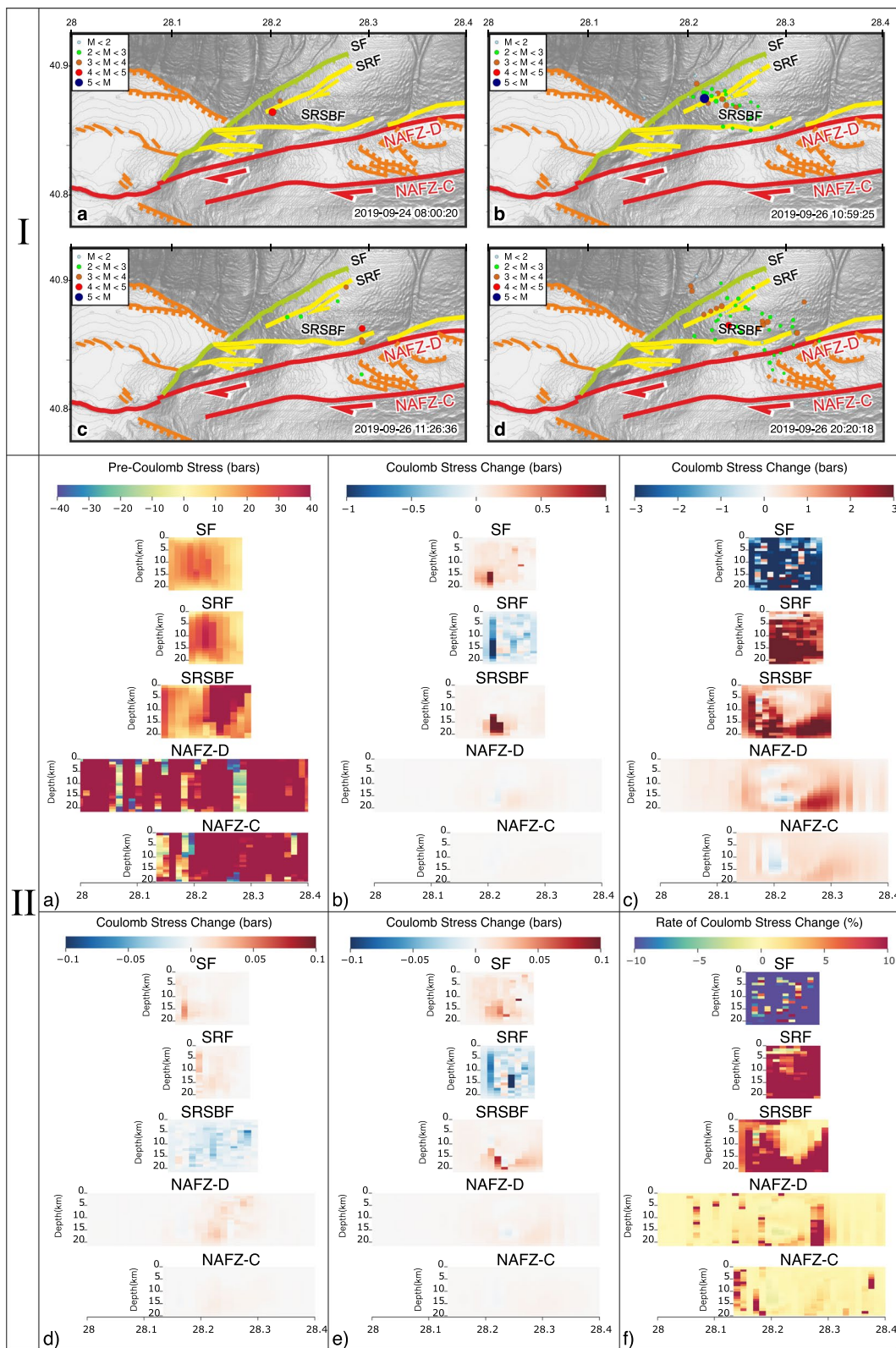
Fig. 6 (See legend on previous page.)

Şahin *et al. Earth, Planets and Space*   (2022) 74:167

Page 12 of 16

earthquakes occurred in a sinistral stepover transpressional zone that formed between two E–W oriented dextral strike-slip faults. They suggested that the mainshock reactivated a WNW–ESE striking north-dipping secondary fault (see their Fig. 4). However, this model fully contradicts existing fault maps (Le Pichon et al. 2001; Armijo et al. 2002; Şengör et al. 2014; Additional file 1: Fig. S1). Since the central basin is located in the west, and the pressure ridge is located in the east, a thrust fault dipping towards NW, as suggested by Irmak et al. (2021), is not plausible in terms of structural geology. Furthermore, our dense seismic profile grid clearly showed that the fault geometries and tectonic models proposed by Karabulut et al. (2021) and Irmak et al. (2021) could not be located in the region (Fig. 4a and Additional file 1: Fig. S6).

There is intense background seismicity across the Marmara region (Fig. 1a). This seismic activity strongly suggests that there are many seismically active faults in the region (e.g., 287 historical earthquakes have been reported for the last 15 centuries (Guidoboni et al. 1994, 2005; Ambraseys 2009). Thirty-seven of these earthquakes, which were likely generated by superimposed major fault segments (Fig. 1a segments from A to G), were severely destructive in at least two large settlements (Yaltırak 2015; Bulut et al. 2019). Apart from the devastating earthquakes in the Marmara region, there is not much information on the whereabouts of the less damaged or non-destructive earthquakes. However, in the fault map, we have produced for the Marmara Sea, there are 66 faults with different characteristics. The length of these faults varies between 2 and 10 km, which can be seen as active traces in the bathymetry (Fig. 1a). In addition to these faults, there are also two NW–SE striking ~50-km-long normal faults (Fig. 1a). Except for the 37 destructive historical earthquakes in the main segments, it is obvious that the rest of the reported historical events occurred on these 68 faults. The 1894 M6.9 Adalar, the 1935 M6.4 Marmara Island, and the 1963 M6.3 Çınarcık earthquakes are known to generated by secondary faults in the Marmara Sea (Altınok and Alpar 2006; Bulut and Aktar 2007; Yaltırak and Şahin 2017). Similar to these earthquakes, the 2019 Silivri earthquakes occurred on secondary faults. Basically, secondary faults deform at much slower rates than their main fault system, resulting in very long recurrence periods of failure. This is well documented by the historical earthquake records indicating 250 moderate size earthquakes in the Marmara region for the time period 500–2019 (Pınar and Lahn 1952; Ergin et al. 1967; Ambraseys and Finkel 1995; Ürekli 1999; Zachariadou 1999; Ambraseys and Jackson 2000; Demirkent 2000; Karacakaya 2000; Ozansoy 2001; Sancaklı 2004; Karagöz 2005; Ambraseys 2009; Yaltırak 2015). In this frame, the 2019 Silivri earthquakes provide

evidence to verify the structural complexity of the NAFZ in the Marmara region.

The modeled Coulomb stress change in response to M4+ earthquakes displays a triggering relation between secondary faults during the 2019 Silivri earthquakes. The slip distribution geometry of the source fault affects the geometry of the redistributed stress on the receiver faults. Nevertheless, the redistributed stress coincides with regions, where the pre-Coulomb stress reaches the maximum on the surfaces of the secondary fault system. The rate of overall stress change on the main segments (NAFZ-C and NAFZ-D) is reaching its maximum, where the pre-Coulomb stress is relatively low along the fault surface. The microseismic activity is observable, where the overall stress change is reaching its maximum on the NAFZ-D (Figs. 5, 6f, Additional file 1: Figs. S10a–c, S11). In addition, the stress-increased fault patches display concordance with aftershock activity (Figs. 5, 6, Additional file 1: Figs. S9, S10). The westward migration of M7+ earthquakes along the NAFZ has terminated right in the eastern edge of the Marmara seismic gap during the 1999 Izmit earthquake. According to our calculations, the 2019 Silivri earthquakes have substantially increased the Coulomb stress on the main segment of the NAFZ in Marmara (up to 3.4 bars), which has not activated since May 1766 and, therefore, will probably prepone one of the future members of westward migrating M7+ earthquakes. Our pre-Coulomb stress calculation results show some (dis)similarities with seismic hazard assessment studies in the Marmara Sea (e.g., Parsons et al. 2000; Parsons 2004; Armijo et al. 2005; Pondard et al. 2007). The dissimilarities between the Coulomb stress model are mainly caused by the location of the last known earthquakes and fault maps, the basis of the study. Our modeled coseismic stress change in response to the 17 August 1999 earthquake shows similar stress rates presented by Parsons (2004), which shows high-stress perturbation on fault segments between Armutlu Peninsula and İstanbul (Fig. 1a, b). Although our modeling results differentiate for the Çınarcık and Tekirdağ basins from the calculated stress rates by Armijo et al. (2005) and Pondard et al. (2007), because the locations of several historical events and estimated rupture lengths are different (Fig. 2), the calculated pre-Coulomb stress rates on the fault surface have not been reactivated since May 1766 in agreement. The change in the estimated rupture length of the 1912 earthquake caused a %15 difference in the stress rate, where the 2019 Silivri earthquakes occurred along the north of the NAFZ-D. This shows that the debated rupture length of the 1912 earthquake has no significant effect on the study area.

Şahin *et al. Earth, Planets and Space*   (2022) 74:167

Page 13 of 16

Conclusions

Previous fault maps constructed using limited seismic profiles immediately after the 1999 earthquakes do not provide the required resolution of the fault architecture to resolve the 2019 Silivri–İstanbul earthquakes. Before the 1999 earthquakes, the number of reliably located moderate-sized earthquakes was not sufficient. The locations and focal mechanism solutions of the Silivri earthquakes verify that the NAFZ has a complex structure in the Marmara Sea.

The joint analysis of the detailed fault map, precise hypocenter locations, source mechanism solutions, and Coulomb stress modeling showed that the 2019 Silivri earthquakes are successive events developed by neighboring and interrelated secondary faults on a pressure ridge in the north of the northern branch of the NAFZ. The M5.8 mainshock took place on a SW–NE striking SE dipping oblique dextral fault where the M4.7 foreshock caused a substantial stress increase, where the mainshock nucleated. The aftershocks of M5.8 also occured on the secondary fault surfaces after the stress increase caused by the mainshock.

As verified by the 2019 Silivri earthquakes, the secondary fault systems in the Marmara Sea can produce moderate-sized earthquakes. In this context, a detailed investigation of secondary fault systems gains importance in determining the earthquake hazard of the highly populated Marmara region.

Abbreviations
NAFZ: North Anatolian Fault Zone; TWT: Two-way travel time.

Supplementary Information

The online version contains supplementary material available at https://doi.org/10.1186/s40623-022-01706-2.

Additional file 1: Figure S1. Fault maps from the previous studies. a) Le Pichon et al. (2001) b) Armijo et al. (2005) c) Yaltırak (2002) d) Şengör et al. (2014). Red-colored rectangular areas show the vicinity of the 2019 Silivri earthquakes, and inset maps show the study area. In figures a, b, and d, there is no mapped fault in the vicinity of Silivri earthquakes, but in figure c, there are two faults that can be seen parallel to each other in the north of the main fault zone. **Figure S2.** 3D fault model for Marmara region with seismicity. The fault model was generated by using the extensive seismic reflection profiles and using the crustal and P-wave velocity models across the Marmara Sea. The earthquakes were adopted from Wollin et al. (2018). The 3D fault geometries are modeled until the depth is 20 km, which is in accordance with the seismogenic depth of the area. **Figure S3.** a) The locations of the seismic sections and fault map. The fault map was gathered by merging the faults on the seismic sections with lineaments and structures on the bathymetric image. b) and c) high-resolution bathymetric images with different colors and display lineaments and structures around where the fault formed. d) shows the interpreted and uninterpreted seismic sections. Seismic sections 1 to 6 were adopted from Steckler et al. (2018) and section 7 from Parke et al. (2003). We have not shown all of the seismic sections in-depth in the figure. The reason for this is that the resolution decreases when the whole section is shown on the vertical scale. The seismic profiles are shown in the figure penetrate to 5

---

seconds. **Figure S4.** The seismicity one–km around the seismic reflection profile that penetrates up to 10 seconds. The seismic reflection profile was adopted from Demirbağ (2004). **Figure S5.** The uncertainty distribution of hypocenters. The average uncertainties are better than 50, 57, and 83 m in E–W, N–S, and U–D directions, respectively. **Figure S6.** Spatiotemporal evolution of the 2019 Silivri earthquakes around vicinity faults. The colors of the faults are the same as in Figure 3 in the main text. The interactive figure lets readers visualize the earthquake occurrences within the time domain by using the "Play" button. The readers can also hide and show the fault geometries and earthquake groups by simply clicking the buttons in the "Explanation" pane in the figure. E.g., If the users want to see the relation between the 2019 Silivri earthquakes and the single fault model of Le Pichon et al. (2001), they can hide the following faults: KBIF, SF, NAFZ-C, SRF, SRSBF, and KBNBF by simply clicking the buttons mentioned faults. Likewise, when all the fault geometries are turned on, the relationship of the fault map presented in this study with the 2019 Silivri earthquakes can be seen. (https://files.codeocean.com/files/verified/8d1a2a29-7204-490b-9acd-30b854684858_v4.0/results.c2eceea7-53ff-4aa5-b2fd-3de0fffb9e91/Figure_S5.html). **Figure S7.** Source mechanism solution of the 2019 Silivri earthquakes with 3D fault model. Blue-colored source mechanism solutions result from this study (Table S1) and red-colored ones from the recent study by Karabulut et al. (2021). In this interactive figure, the readers can hide and display the faults from the Explanation pane. E.g., if the readers wish to see the relation between the single fault model and source mechanism solutions, the readers should hide the KBIF, SF, NAFZ-C, SRF, SRSBF, and KBNBF by clicking the buttons next to fault names. When the all-fault geometries are visualized, it can be seen which fault solutions are on the fault geometries presented in this study. Thus, the focal mechanism solutions of two different studies can be comparable. Furthermore, the readers can also compare which fault model is more realistic by considering the focal mechanism solutions of two other studies. (https://files.codeocean.com/files/verified/8d1a2a29-7204-490b-9acd-30b854684858_v4.0/results.c2eceea7-53ff-4aa5-b2fd-3de0fffb9e91/Figure_S6.html). **Figure S8.** Spatial distribution of the 2019 Silivri earthquakes from another recent study by Durand et al. (2020) with a 3D fault model for comparison with Figure S5. In this figure, fault geometries and earthquake groups can be hidden by clicking the buttons in the Explanation pane. If the readers wish to see the single fault model with earthquake location provided by Durand et al. (2020), the readers should hide the following faults: KBIF, SF, NAFZ-C, SRF, SRSBF, and KBNBF. As shown in the figure, the earthquake location provided by Durand et al. (2020) correlates well with the fault geometries presented in this study. (https://files.codeocean.com/files/verified/8d1a2a29-7204-490b-9acd-30b854684858_v4.0/results.c2eceea7-53ff-4aa5-b2fd-3de0fffb9e91/Figure_S7.html). **Figure S9.** Coseismic stress changes the receiver faults as a response to M4+ earthquakes and slip distribution on the source fault. a) k-square (https://files.codeocean.com/files/verified/8d1a2a29-7204-490b-9acd-30b854684858_v4.0/results.c2eceea7-53ff-4aa5-b2fd-3de0fffb9e91/Figure_S8a.html), b) bulls-eye (https://files.codeocean.com/files/verified/8d1a2a29-7204-490b-9acd-30b854684858_v4.0/results.c2eceea7-53ff-4aa5-b2fd-3de0fffb9e91/Figure_S8b.html) and c) uniform slip (https://files.codeocean.com/files/verified/8d1a2a29-7204-490b-9acd-30b854684858_v4.0/results.c2eceea7-53ff-4aa5-b2fd-3de0fffb9e91/Figure_S8c.html) models. **Figure S10.** Pre-Coulomb stress, cumulative stress change, and the stress change rate on the vicinity faults of the 2019 Silivri earthquakes. The first pane in each subfigure indicates the pre-Coulomb stress on the faults derived from slip deficit. The second pane shows the cumulative stress change on the vicinity fault in response to M4+ earthquakes, and the third pane displays the stress change rate. Both cumulative and rate of stress change exhibit alternation according to the slip geometry a) k-square (https://files.codeocean.com/files/verified/8d1a2a29-7204-490b-9acd-30b854684858_v4.0/results.c2eceea7-53ff-4aa5-b2fd-3de0fffb9e91/Figure_S9a.html), b) bulls-eye (https://files.codeocean.com/files/verified/8d1a2a29-7204-490b-9acd-30b854684858_v4.0/results.c2eceea7-53ff-4aa5-b2fd-3de0fffb9e91/Figure_S9b.html), and c) uniform slip (https://files.codeocean.com/files/verified/8d1a2a29-7204-490b-9acd-30b854684858_v4.0/results.c2eceea7-53ff-4aa5-b2fd-3de0fffb9e91/Figure_S9c.html) models. **Figure S11.** The confining pressure change in response to the M5.8 mainshock during the 2019 Silivri earthquakes. The aftershock activity is in agreement with the increased confining pressure that is correlated with pore pressure

Şahin *et al. Earth, Planets and Space*   (2022) 74:167

Page 14 of 16

change (https://files.codeocean.com/files/verified/8d1a2a29-7204-490b-9acd-30b854684858_v4.0/results.c2eceea7-53ff-4aa5-b2fd-3de0fffb9e91/Figure_S10.html). **Table S1.** Source mechanism solution of the Silivri earthquakes larger than M 3.

Availability of data and materials
The data resulting from this research and interactive figure generation codes reside in the Code Ocean portal with https://doi.org/10.24433/CO.3945023 (https://codeocean.com/capsule/4986058). The interactive figures were generated using Plotly (Plotly Technologies Inc. 2015) in Python. The maps were generated using GMT (Wessel et al. 2013). The earthquake data were combined from Disaster and Emergency Management Presidency of Turkey (AFAD) and Kandilli Observatory and Earthquake Research Institute (KOERI).

Declarations

Ethics approval and consent to participate
Not applicable.

Consent for publication
Not applicable.

Competing interests
The authors declare that they have no conflict of interest.

Author details
[1]Department of Geological Engineering, Faculty of Mines, Istanbul Technical University, Istanbul, Turkey. [2]Department of Geodesy, Boğaziçi University, Kandilli Observatory and Earthquake Research Institute, Istanbul, Turkey.

References
Steckler MS, Cifci G, Demirbag E, et al (2018) Processed multichannel seismic data in the Marmara Sea, acquired during the R/V Koca Piri Reis survey in 2008 as part of the Turkish-American Marmara Multichannel Project (TAMAM). https://doi.org/10.1594/IEDA/500159

Aksoy ME, Meghraoui M, Vallée M, Çakir Z (2010) Rupture characteristics of the A.D. 1912 Mürefte (Ganos) earthquake segment of the North Anatolian fault (western Turkey). Geology 38:991–994. https://doi.org/10.1130/G31447.1

Aksu AE, Calon TJ, Hiscott RN, Yasar D (2000) Anatomy of the North Anatolian fault zone in the Marmara Sea, Western Turkey: extensional basins above a continental transform. GSA Today 10:3–7

Altınok Y, Alpar B (2006) Marmara Island earthquakes, of 1265 and 1935; Turkey. Nat Hazards and Earth Syst Sci 6:999–1006. https://doi.org/10.5194/nhess-6-999-2006

Altınok Y, Alpar B, Yaltırak C (2003) Şarköy-Mürefte 1912 earthquake's tsunami, extension of associated faulting in the Marmara Sea, Turkey. J Seismol 3:329–346. https://doi.org/10.1023/A:1024581022222

Ambraseys N (2009) Earthquakes in the Mediterranean and Middle East: a multidisciplinary study of seismicity up to 1900. Cambridge University Press

Ambraseys NN, Finkel C (1995) The seismicity of Turkey and adjacent areas: a historical review, 1500–1800. Eren Yayıncılık ve Kitapcılık Ltd., Istanbul

Ambraseys NN, Jackson JA (2000) Seismicity of the Sea of Marmara (Turkey) since 1500. Geophys J Int 141:F1–F6

Armijo R, Meyer B, Navarro S et al (2002) Asymmetric slip partitioning in the Sea of Marmara pull-apart: a clue to propagation processes of the North Anatolian fault? Terra Nova 14:80–86. https://doi.org/10.1046/j.1365-3121.2002.00397.x

Armijo R, Pondard N, Meyer B et al (2005) Submarine fault scarps in the Sea of Marmara pull-apart (North Anatolian Fault): implications for seismic hazard in Istanbul. Geochem, Geophys, Geosyst. https://doi.org/10.1029/2004GC000896

Ateş A, Kayiran T, Sincer I (2003) Structural interpretation of the Marmara region, NW Turkey, from aeromagnetic, seismic and gravity data. Tectonophysics 367:41–99. https://doi.org/10.1016/S0040-1951(03)00044-1

Barbot S, Fialko Y (2010a) Fourier-domain Green's function for an elastic semi-infinite solid under gravity, with applications to earthquake and volcano deformation. Geophys J Int 182:568–582. https://doi.org/10.1111/j.1365-246X.2010.04655.x

Barbot S, Fialko Y (2010b) A unified continuum representation of post-seismic relaxation mechanisms: semi-analytic models of afterslip, poroelastic rebound and viscoelastic flow. Geophys J Int 182:1124–1140. https://doi.org/10.1111/j.1365-246X.2010.04678.x

Barbot S (2014) Relax v1.0.7. Computational infrastructure for geodynamics. https://geodynamics.org

Barka A, Akyüz HS, Altunel E et al (2002) The surface rupture and slip distribution of the 17 August 1999 Izmit Earthquake (M 7.4), North Anatolian Fault. Bull Seismol Soc Am 92:43–60. https://doi.org/10.1785/0120000841

Barka AA (1992) The north Anatolian fault zone. In: Annales tectonicae. pp 164–195

Batsi E, Lomax A, Tary J et al (2018) An Alternative view of the microseismicity along the western main marmara fault. Bull Seismol Soc Am 108:2650–2674. https://doi.org/10.1785/0120170258

Bayrakçı G, Laigle M, Bécel A et al (2013) 3-D sediment-basement tomography of the Northern Marmara trough by a dense OBS network at the nodes of a grid of controlled source profiles along the North Anatolian fault. Geophys J Int 194:1335–1357. https://doi.org/10.1093/gji/ggt211

Beeler NM, Tullis TE, Blanpied ML, Weeks JD (1996) Frictional behavior of large displacement experimental faults. J Geophys Res Solid Earth 101:8697–8715. https://doi.org/10.1029/96JB00411

Bulut F, Bohnhoff M, Ellsworth WL et al (2009) Microseismicity at the North Anatolian Fault in the Sea of Marmara offshore Istanbul, NW Turkey. J Geophys Res Solid Earth 114:9302. https://doi.org/10.1029/2008JB006244

Bulut F, Aktuğ B, Yaltırak C et al (2019) Magnitudes of future large earthquakes near Istanbul quantified from 1500 years of historical earthquakes, present-day microseismicity and GPS slip rates. Tectonophysics 764:77–87. https://doi.org/10.1016/j.tecto.2019.05.005

Bulut F, Aktar M (2007) Accurate relocation of İzmit earthquake (Mw= 7.4, 1999) aftershocks in Çınarcık Basin using double difference method. Geophys Res Lett 34:L10307. https://doi.org/10.1029/2007GL029611

Carton H, Singh SC, Hirn A et al (2007) Seismic imaging of the three-dimensional architecture of the Çınarcık Basin along the North Anatolian Fault. J Geophys Res Solid Earth 112:6101. https://doi.org/10.1029/2006JB004548

Demirbağ E, Kurt H, Düşünür D et al (2007) Constructing a 3D structural block diagram of the Central Basin in Marmara Sea by means of bathymetric and seismic data. Mar Geophys Res 28:343–353. https://doi.org/10.1007/S11001-007-9036-3/FIGURES/8

Demirkent I (2000) Bizans kaynaklarna göre IV–XI yüzyllarda Istanbul ve çevresinde depremler. Tarih Boyunca Anadoluda Dogal Afetler ve Deprem Semineri, 22–23

Dix CH (1955) Seismic velocities from surface measurements. Geophysics 20:68–86. https://doi.org/10.1190/1.1438126

Durand V, Bentz S, Kwiatek G et al (2020) A two-scale preparation phase preceded an Mw 5.8 earthquake in the Sea of Marmara Offshore Istanbul.

Turkey Seismol Res Lett 91:3139–3147. https://doi.org/10.1785/0220200110

Egeran EN, Lahn E (1948) Türkiye Jeolojisi. Ankara

Egeran EN, Lahn E (1944) Note su la Carte Sismique de la Turquie au 1:2.400.000. Bull Miner Res Exploration 32:279–289

Ergin K, Güçlü U, Uz Z (1967) Türkiye ve civarinin deprem katalogu, Istanbul: Maden Fak. Arz Fizigi Enst Yay Istanbul 24:169

Gallovič F, Brokešová J (2004) On strong ground motion synthesis with k-2 slip distributions. J Seismol 8:211–224. https://doi.org/10.1023/B:JOSE.0000021438.79877.58

Geller RJ, Mueller CS (1980) Four similar earthquakes in central California. Geophys Res Lett 7:821–824. https://doi.org/10.1029/GL007i010p00821

Guidoboni E, Comastri A, Traina G (1994) Catalogue of ancient earthquakes in the mediterranean area up to the 10th century. Istituto nazionale di geofisica e vulcanologia, Rome

Guidoboni E, Comastri A, Phillips B (2005) Catalogue of earthquakes and tsunamis in the mediterranean area from the 11th to the 15th century. Istituto nazionale di geofisica e vulcanologia, Rome

Gürbüz C, Aktar M, Eyidoğan H et al (2000) The seismotectonics of the Marmara region (Turkey): results from a microseismic experiment. Tectonophysics 316:1–17. https://doi.org/10.1016/S0040-1951(99)00253-X

Hanks TC, Kanamori H (1979) A moment magnitude scale. J Geophys Res 84:2348. https://doi.org/10.1029/JB084iB05p02348

Hubert-Ferrari A, Barka A, Jacques E et al (2000) Seismic hazard in the Marmara Sea region following the 17 August 1999 Izmit earthquake. Nature 404:269–273. https://doi.org/10.1038/35005054

Irmak TS, Yolsal-Çevikbilen S, Eken T et al (2021) Source characteristics and seismotectonic implications of the 26 September 2019 M w 5.7 Silivri High-Kumburgaz Basin earthquake and evaluation of its aftershocks at the North Anatolian Fault Zone (Central Marmara Sea, NW Turkey). Geophys J Int 227:383–402. https://doi.org/10.1093/gji/ggab233

Karabulut H, Bouin M-P, Bouchon M et al (2002) The Seismicity in the Eastern Marmara Sea after the 17 August 1999 Izmit Earthquake. Bull Seismol Soc Am 92:387–393. https://doi.org/10.1785/0120000820

Karabulut H, Güvercin SE, Eskiköy F et al (2021) The moderate size 2019 September Mw 5.8 Silivri earthquake unveils the complexity of the Main Marmara Fault shear zone. Geophys J Int 224:377–388. https://doi.org/10.1093/gji/ggaa469

Karacakaya R (2000) Şarköy-Mürefte Depremi (1912). Tarih Boyunca Anadolu'da Doğal Afetler ve Deprem Semineri 203–218

Karagöz Ş (2005) Eskiçağ'da depremler. Türk Eskiçağ Bilimleri Enstitüsü Yayınları

Ketin İ (1948) Über die tektonisch-mechanischen Folgerungen aus den großen anatolischen Erdbeben des letzten Dezenniums. Geol Rundsch 36:77–83

Kurt H, Yücesoy E (2009) Submarine structures in the Gulf of İzmit, based on multichannel seismic reflection and multibeam bathymetry. Mar Geophys Res 30:73–84. https://doi.org/10.1007/s11001-009-9068-y

Le Pichon X, Şengör AMC, Demirbağ E et al (2001) The active Main Marmara Fault. Earth Planet Sci Lett 192:595–616. https://doi.org/10.1016/S0012-821X(01)00449-6

Mildon ZK, Toda S, Faure Walker JP, Roberts GP (2016) Evaluating models of Coulomb stress transfer: is variable fault geometry important? Geophys Res Lett 43:12407–12414. https://doi.org/10.1002/2016GL071128

Mildon ZK, Roberts GP, Faure Walker JP, Toda S (2019) Coulomb pre-stress and fault bends are ignored yet vital factors for earthquake triggering and hazard. Nat Commun 10:1–9. https://doi.org/10.1038/s41467-019-10520-6

Okay S, Aydemir S (2016) Control of active faults and sea level changes on the distribution of shallow gas accumulations and gas-related seismic structures along the central branch of the North Anatolian Fault, southern Marmara shelf, Turkey. Geodin Acta 28:328–346. https://doi.org/10.1080/09853111.2016.1183445

Okay Aİ, Kaşlılar-Özcan A, Imren C et al (2000) Active faults and evolving strike-slip basins in the Marmara Sea, northwest Turkey: a multichannel seismic reflection study. Tectonophysics 321:189–218. https://doi.org/10.1016/S0040-1951(00)00046-9

Örgülü G (2011) Seismicity and source parameters for small-scale earthquakes along the splays of the North Anatolian Fault (NAF) in the Marmara Sea. Geophys J Int 184:385–404. https://doi.org/10.1111/j.1365-246X.2010.04844.x

Ozansoy E (2001) Bizans kaynaklarna göre 1200–1453 İstanbul depremleri. Tarih Boyunca Anadolu'da Dogal Afetler ve Deprem Semineri Bildiriri Kitabı, 1–29

Parke JR, White RS, McKenzie D et al (2003) The Sea of Marmara: a two-dimensional seismic reflection profile data archive. Geochem Geophys Geosyst 4:1084. https://doi.org/10.1029/2002GC000493

Parsons T (2004) Recalculated probability of M ≥ 7 earthquakes beneath the Sea of Marmara. Turkey J Geophys Res Solid Earth 109:5304. https://doi.org/10.1029/2003JB002667

Parsons T, Toda S, Stein RS et al (2000) Heightened odds of large earthquakes near Istanbul: an interaction-based probability calculation. Science 288:661–665. https://doi.org/10.1126/science.288.5466.661

Pınar N, Lahn E (1952) Türkiye depremleri izahı kataloğu. Bayndırlık Bakanlğı, Yapı ve İmar İşleri Reisliği 6:

Plotly Technologies Inc. (2015) Collaborative data science. https://plotly.com

Pondard N, Armijo R, King GCP et al (2007) Fault interactions in the Sea of Marmara pull-apart (North Anatolian Fault): earthquake clustering and propagating earthquake sequences. Geophys J Int 171:1185–1197. https://doi.org/10.1111/j.1365-246X.2007.03580

Rangin C, Demirbag E, Imren C, et al (2001) Marine Atlas of the Sea of Marmara (Turkey). Data collected on board R. V Le Suroît, September 2000

Sancaklı N (2004) Marmara Bölgesi depremleri, MÖ 427-MS 1912. Kastaş Yaynevi

Şengör AMC (1979) The North Anatolian transform fault: its age, offset and tectonic significance. J Geol Soc London 136:269–282. https://doi.org/10.1144/gsjgs.136.3.0269

Şengör AMC, Grall C, İmren C et al (2014) The geometry of the North Anatolian transform fault in the Sea of Marmara and its temporal evolution: implications for the development of intracontinental transform faults. Can J Earth Sci 51:222–242. https://doi.org/10.1139/cjes-2013-0160

Siyako M, Tanış T, Şaroğlu F (2000) Marmara Denizi'nin Aktif Fay Geometrisi. Bilim Ve Teknik 388:66–71

Snoke A (2003) Focal mechanism determination software (FOCMEC package) 388:67

Sorlien CC, Akhun SD, Seeber L et al (2012) Uniform basin growth over the last 500 ka, North Anatolian Fault, Marmara Sea, Turkey. Tectonophysics 518:1–16. https://doi.org/10.1016/j.tecto.2011.10.006

Sylvester AG (1988) Strike-slip faults. Geol Soc Am Bull 100:1666–1703. https://doi.org/10.1130/0016-7606(1988)100<1666:SSF>2.3.CO;2

Tary JB, Geli L, Henry P et al (2011) Sea-bottom observations from the Western Escarpment of the Sea of Marmara. Bull Seismol Soc Am 101:775–791. https://doi.org/10.1785/0120100014

Tchalenko JS (1970) Similarities between shear zones of different magnitudes. Bull Seismol Soc Am 81:1625–1640. https://doi.org/10.1130/0016-7606(1970)81[1625:SBSZOD]2.0.CO;2

Ürekli F (1999) İstanbul'da 1894 depremi. İletişim

Vardar D, Öztürk K, Yaltırak C et al (2014) Late Pleistocene-Holocene evolution of the southern Marmara shelf and sub-basins: middle strand of the North Anatolian fault, southern Marmara Sea. Turkey Marine Geophys Res 35:69–85. https://doi.org/10.1007/s11001-013-9210-8

Waldhauser F, Ellsworth WL (2000) A double-difference earthquake location algorithm: method and application to the Northern Hayward Fault. California Bull Seismol Soc Am 90:1353–1368. https://doi.org/10.1785/0120000006

Wessel P, Smith WHF, Scharroo R et al (2013) Generic mapping tools: improved version released. Eos (washington DC) 94:409–410. https://doi.org/10.1002/2013EO450001

Wollin C, Bohnhoff M, Martínez-Garzón P et al (2018) A unified earthquake catalogue for the Sea of Marmara Region, Turkey, based on automatized phase picking and travel-time inversion: Seismotectonic implications. Tectonophysics 747–748:416–444. https://doi.org/10.1016/j.tecto.2018.05.020

Xu H, Xu S, Nieto-Samaniego ÁF, Alaniz-Álvarez SA (2017) Slicken 1.0: program for calculating the orientation of shear on reactivated faults. Comput Geosci 104:158–165. https://doi.org/10.1016/j.cageo.2016.07.015

Yaltırak C (2002) Tectonic evolution of the Marmara Sea and its surroundings. Mar Geol 190:493–529. https://doi.org/10.1016/S0025-3227(02)00360-2

Yaltırak C (2015) Marmara Denizi ve Çevresinde Tarihsel Depremlerin Yerleri ve Anlamı. İtü Vakfı Dergisi 67:51–58

Yaltırak C, Alpar B (2002) Evolution of the middle strand of North Anatolian Fault and shallow seismic investigation of the southeastern Marmara

Sea (Gemlik Bay). Mar Geol 190:307–327. https://doi.org/10.1016/S0025-3227(02)00352-3

Yaltırak C, Şahin M (2017) 10th of July, 1894 Istanbul earthquake (Marmara Sea, Turkey). In: EGU general assembly conference abstracts. p 12465

Zachariadou EA (1999) Natural disasters in the Ottoman Empire: Halcyon Days in Crete III: a symposium held in Rethymnon 10–12 January 1997. Crete University Press

Publisher's Note